Effects of orthogonal rotating electric fields on electrospinning process

M. Lauricella, F. Cipolletta, G. Pontrelli, D. Pisignano, and S. Succi

Citation: Physics of Fluids **29**, 082003 (2017); doi: 10.1063/1.4997086
View online: http://dx.doi.org/10.1063/1.4997086
View Table of Contents: http://aip.scitation.org/toc/phf/29/8
Published by the American Institute of Physics

Effects of orthogonal rotating electric fields on electrospinning process

M. Lauricella,[1,a)] F. Cipolletta,[1] G. Pontrelli,[1] D. Pisignano,[2,3] and S. Succi[1,4,b)]
[1]*Istituto per le Applicazioni del Calcolo CNR, Via dei Taurini 19, IT 00185 Rome, Italy*
[2]*Dipartimento di Matematica e Fisica "Ennio De Giorgi," University of Salento, Via Arnesano, IT 73100 Lecce, Italy*
[3]*NEST, Istituto Nanoscienze-CNR, Piazza S. Silvestro 12, IT 56127 Pisa, Italy*
[4]*Institute for Applied Computational Science, Harvard "John A. Paulson" School of Engineering and Applied Sciences, Cambridge, Massachusetts 02138, USA*

(Received 9 May 2017; accepted 20 July 2017; published online 8 August 2017)

Electrospinning is a nanotechnology process whereby an external electric field is used to accelerate and stretch a charged polymer jet, so as to produce fibers with nanoscale diameters. In quest of a further reduction in the cross section of electrified jets hence of a better control on the morphology of the resulting electrospun fibers, we explore the effects of an external rotating electric field orthogonal to the jet direction. Through intensive particle simulations, it is shown that by a proper tuning of the electric field amplitude and frequency, a reduction of up to a 30% in the aforementioned radius can be obtained, thereby opening new perspectives in the design of future ultra-thin electrospun fibers. Applications can be envisaged in the fields of nanophotonic components as well as for designing new and improved filtration materials. *Published by AIP Publishing.* [http://dx.doi.org/10.1063/1.4997086]

I. INTRODUCTION

Electrospinning has witnessed a dramatic upsurge of interest in recent years because of its potential to produce ultrafine fibers with sub-micrometer diameters (see Refs. 1–7). Though routinely realizable in the laboratory, electrospinning is a complex phenomenon to analyze because of the coupling between the electric field and the non-linear deformation of the fluid, the latter being dictated by the rheology of the material. As a consequence, the resulting jet (fiber) diameter is affected by several material, design, and operating parameters.

In this context, computational models represent a useful tool to investigate the underlying physics of electrospinning and provide information which may be used for the design of new electrospinning experiments and nanofibrous materials. Several strategies have been pursued to model the process, which can be broadly classified within two main families, Eulerian and Lagrangian. The former is based on a fixed-grid discretization of the partial differential equations of continuum fluid-dynamics,[8–11] while in the latter, the grid moves with the flow, taking the form of particle-like ordinary differential equations.[12–15]

By using suitable theoretical models, the effects of the parameters on the fiber diameter can be systematically studied and assessed, both analytically and numerically. For example, it has been shown that bending (or whipping) instabilities of electrical and hydrodynamical nature are mostly responsible for jet stretching during the electrospinning process.[12,16,17] This behavior leads to a reduction of the cross section radius of electrospun nanofibers. In other studies, the attention is mostly focused on the morphological aspects, revealing a wide variety of pattern depositions of electrified jets.[16,18] In the literature, one can find theoretical models to describe the jet dynamics and control of the fiber diameter, through numerical simulations based on multi-parameter choice, involving the perturbation at the nozzle, the intensity of the fixed electric field, and the density of the polymer solution.[12,18,19] However, investigating new strategies to improve the overall control on electrospun nanofibrous materials is still an open scientific and technological challenge. In the present work, we consider the effect of a rotating electric field orthogonal to the main electric field (Fig. 1). In particular, we present a theoretical model and ensuing numerical simulations with the JETSPIN code,[20,21] in order to identify the optimal values of the amplitude and rotational frequency of the orthogonal rotating electric field (OREF), which permit to alter fiber morphology.

II. THE MODEL

The jet emitted by the nozzle is modeled by a finite set of n parcels at a distance l_i [distance between the ith and $(i+1)$th parcels], connected via viscoelastic elements, similarly to previous electrospinning models.[12,14,22,23] Each jet parcel represents a cylindrical element of jet volume $V_i = V_0$ and initial height $l_i = l_{step}$ (initial length step of jet discretization). As a consequence, the initial radius R_0 of the jet element is equal to $\sqrt{V_0/\pi l_{step}}$. From this representation, the following set of equations of motion (EOM) can be written for each parcel i (hereafter, we shall consider the x-axis pointing from the nozzle to the collector):

$$\frac{d\vec{r}_i}{dt} = \vec{v}_i, \tag{1}$$

$$\frac{d\sigma_i}{dt} = \frac{G}{l_i}\frac{dl_i}{dt} - \frac{G}{\mu}\sigma_i, \tag{2}$$

a)Email: m.lauricella@iac.cnr.it
b)Author to whom correspondence should be addressed: s.succi@iac.cnr.it

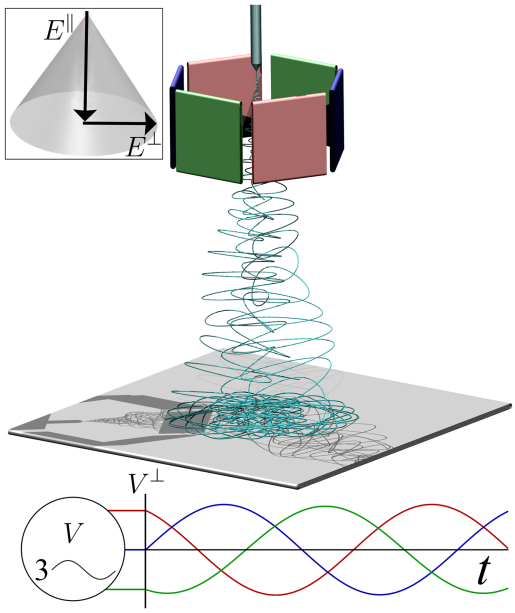

FIG. 1. Sketch representation of the electrospinning process in the presence of an orthogonal rotating electric field (OREF). The jet, ejected from a nozzle, is stretched by an electric field $E_{\parallel}$ parallel to the x axis. The OREF $E_{\perp}$ can be generated by a series of capacitor plates hexagonally arranged and connected to a three-phase power source. The electrical power source is graphically represented in the bottom part of the figure. Here, the three-phase voltage shows colors corresponding to the color of the connected capacitor plate.

$$m_i \frac{d\vec{v}_i}{dt} = q_i \vec{E} + \sum_{j \neq i} \left(\frac{q_i q_j}{|\vec{r}_j - \vec{r}_i|^2} \vec{u}_{i,j} \right) - \pi {R_i}^2 \sigma_i \vec{t}_i + \pi {R_{i+1}}^2 \sigma_{i+1} \vec{t}_{i+1} + k_i \, \pi \left(\frac{R_i + R_{i+1}}{2} \right)^2 \alpha \, \vec{c}_i. \quad (3)$$

In the above, the subscript i stands for the ith parcel, $\vec{r}_i$ is the position vector, $\vec{v}_i$ is the velocity vector, G is the elastic modulus, μ is the viscosity of the fluid jet, σ is the stress, R is the cross sectional radius, q is the charge, $\vec{E}$ is the electric field (Fig. 1), $\vec{u}_{i,j}$ is the unit vector from parcel i to parcel j, $\vec{t}_i$ is the unit vector pointing from parcel i to $(i-1)$, k_i is the local curvature, α is the surface tension coefficient, and $\vec{c}_i$ is the unit vector pointing from parcel i to the local centre of curvature. It is worth stressing that the filament radius R_i at each ith parcel location is equal to $\sqrt{V_0/\pi l_i}$, as a result of the volume conservation. Note that the constitutive Eq. (2) models a Maxwell material with constant viscosity, in line with the approach of Refs. 12 and 22.

The aforementioned system of EOM is numerically solved, starting each simulation with only two bodies: a parcel fixed at $x = 0$, representing the spinneret nozzle, and a second parcel modeling the initial jet segment located at distance l_{step} from the nozzle along the x axis with a given initial velocity v_i° (defined below). Once the last parcel reaches a distance $2l_{step}$ away from the nozzle, a new parcel (third body) is placed at a distance l_{step}, the length step used to discretize the jet as a sequence of parcels. Repeating this injection rule over time, we obtain a set of n discrete jet elements.

The initial velocity is defined as $v_i^{\circ} = v_s + v_{d,i}$, where v_s is a velocity term along the x axis, modeling the bulk fluid velocity in the syringe needle, and $v_{d,i}$ denotes the dragging velocity,

$$v_{d,i} = \frac{v_{i-1} - v_s}{2}. \quad (4)$$

The extra term $v_{d,i}$ accounts for the drag effect of the electrospun jet on the last inserted segment $(i-1)$. Note that the definition of $v_{d,i}$ was chosen in such a way so as to keep the velocity strain unchanged before and after the parcel insertion.

Furthermore, we take into account a periodic nozzle perturbation with frequency ω_{pert} and amplitude A_{pert}, which models fast mechanical oscillations nearby the spinneret. This perturbation results in the emission of a conic helix jet. We are interested in adding an OREF to the above configuration, namely,

$$\vec{E} = \vec{E}^{\parallel} + \vec{E}^{\perp}. \quad (5)$$

Hereafter, the main electric field and the OREF are denoted by $\vec{E}^{\parallel} = (E_x, 0, 0)$ and $\vec{E}^{\perp} = \left(0, E_y, E_z\right)$, respectively. In equations,

$$E_y(A, \omega, t) = A \cos \omega t,$$
$$E_z(A, \omega, t) = A \sin \omega t, \quad (6)$$

where $A(\mathrm{g}^{\frac{1}{2}}\ \mathrm{cm}^{-\frac{1}{2}}\ \mathrm{s}^{-1})$ is the modulus and $\omega(\mathrm{s}^{-1})$ is the angular frequency. OREFs have already been treated in the literature, in the context of plasma confinement by means of a series of capacitor plates with alternating current around the apparatus.[24] In JETSPIN, we modified the EOM according to Eqs. (5) and (6).

With the exception of A and ω, in all simulations we use the numerical parameters proposed in Ref. 20. These values were assessed by comparing with experimental data from an electrospinning process of polyvinylpyrrolidone (molecular weight = 1300 kDa, mixture of ethanol and water 17:3 v:v, with PVP concentration 2.5 wt. %).[25] In particular, we consider the surface tension $\alpha = 21.1\ \mathrm{g\ s^{-2}}$ from Ref. 26, the elastic modulus $G = 5 \cdot 10^4\ \mathrm{g\ cm^{-1}\ s^{-2}}$ from Ref. 27, and the shear viscosity $\mu = 100\,\mu_0$, where μ is taken equal to two orders of magnitude larger than the zero-shear viscosity $\mu_0 = 0.2\ \mathrm{g\ cm^{-1}\ s^{-1}}$, see Refs. 26 and 28. This is because the strong longitudinal flows which we are dealing with can lead to an increase of the extensional viscosity, as observed in the literature.[12,29] Finally, v_s is taken equal to $0.28\ \mathrm{cm\ s^{-1}}$ which corresponds to a constant flow rate of $2\ \mathrm{ml\ h^{-1}}$ in a needle of radius 250 μm.

TABLE I. Parameter values in the simulations.

Simulated time	0.1	s
Discretization length step l_{step}	0.02	cm
Initial jet radius R_0	$5 \cdot 10^{-3}$	cm
Charge density	$4.4 \cdot 10^4$	$\mathrm{g^{\frac{1}{2}}\ cm^{-\frac{3}{2}}\ s^{-1}}$
Fluid viscosity μ	20	$\mathrm{g\ cm^{-1}\ s^{-1}}$
Elastic modulus G	$5 \cdot 10^4$	$\mathrm{g\ cm^{-1}\ s^{-2}}$
Collector distance h	16	cm
External electric potential ($hE^{\parallel}$)	30.021	$\mathrm{g^{\frac{1}{2}}\ cm^{\frac{1}{2}}\ s^{-1}}$
Surface tension α	21.13	$\mathrm{g\ s^{-2}}$
Bulk velocity v_s	0.28	$\mathrm{cm\ s^{-1}}$
Perturbation frequency ω_{pert}	10^4	$\mathrm{s^{-1}}$
Perturbation amplitude A_{pert}	10^{-3}	cm
OREF modulus A	[0.0, 10.0]	$\mathrm{g^{\frac{1}{2}}\ cm^{-\frac{1}{2}}\ s^{-1}}$
OREF frequency ω	[0.5, 20.0]	$\mathrm{10^4\ s^{-1}}$

The values of the simulation parameters are summarized in Table I.

III. RESULTS

In the following, we present an exploratory study of the effects of the amplitude A and frequency ω on the electrospinning process. We wish to emphasize that this does not represent a fully fledged analysis of the non-linear dynamical behaviour of this complex system, but rather a computational identification of the most interesting regions in the $A-\omega$ parameter space.

A. Modulus and frequency of OREF

We investigate the effect of $\vec{E}^{\perp}$ in Eqs. (6), compared to the standard case $\vec{E}^{\parallel}$, and study the way the jet morphology is deformed for different choices of the free-parameters. We take $A^* = |\vec{E}^{\parallel}| \simeq 1.8763\ \mathrm{g}^{\frac{1}{2}}\ \mathrm{cm}^{-\frac{1}{2}}\ \mathrm{s}^{-1}$ and $\omega^* = \omega_{\mathrm{pert}} = 10^4\ \mathrm{s}^{-1}$ as reference values, respectively, for A and ω in Eqs. (6). A wide range of physically relevant values of these parameters is spanned by selecting $A \in [0, 10]$ and $10^{-4}\omega \in [0.5, 20]$ (see Ref. 25). Such high values of the angular frequency ω mediate the OREF along the circumference orthogonal to $\vec{E}^{\parallel}$. Note that the dominant component of the force acting on each parcel is the one given by $\vec{E}^{\parallel}$, since the jet travels towards the collector without undergoing any breakup, such as that reported in the literature.[16]

The two components of the electric field are shown in the top left panel of Fig. 1, where the vertical and horizontal arrows represent $\vec{E}^{\parallel}$ and $\vec{E}^{\perp}$, respectively, while the total field $\vec{E}$ runs over the transparent gray conic surface. We run several simulations, each for a total time of 0.1 s. After an initial drift $t_{\mathrm{drift}} = 0.02$ s, the jet dynamics is assumed regular so that we can estimate mean values of suitable observables over their stationary statistical distributions.[20] In particular, the mean value of the filament radius R was estimated at the collector in different simulations with several pairs of A and ω values. The surface of the mean radius R was reconstructed as a function of A and ω by linear interpolation, shown by contour lines in Fig. 2. It is worth observing that for $A = 0$, the mean cross section radius reduces to $R_0 = 4.05 \cdot 10^{-4}$ cm, in agreement with the mean cross section values obtained for the standard case, $\vec{E} = \vec{E}^{\parallel}$. Further, as a representative value, we analyze the case $A = 5\ \mathrm{g}^{\frac{1}{2}}\mathrm{cm}^{-\frac{1}{2}}\mathrm{s}^{-1}$ in Fig. 3, namely, the red vertical line in Fig. 2. Along such a line, we plot R as a function of ω, together with the corresponding confidence interval (namely, the interquartile interval). In this figure, the thick black horizontal line indicates R_0 allowing a direct comparison between the cases with and without OREF.

From this plot, an oscillatory behavior of R as a function of ω is clearly recognizable. Two representative points are singled out, namely, the first minimum m_1, with $R(m_1) = 2.65 \cdot 10^{-4}$ cm, corresponding to $\omega(m_1) = 2.5 \times 10^4\ \mathrm{s}^{-1}$ and the relative maximum M_1 with $R(M_1) = 4.15 \cdot 10^{-4}$ cm, with $\omega(M_1) = 6 \times 10^4\ \mathrm{s}^{-1}$. The corresponding jet-paths are reported in the sub-panels: one is the view from the side and the other is the view from the collector, looking up to the nozzle. It is worth noting that, although the helix associated with $\omega(M_1)$ is wider than the one for $\omega(m_1)$, the latter is more entangled, meaning that the jet undergoes longer-lived instabilities, resulting in a smaller value of R. 3D representations of the two highlighted trajectories are displayed in Fig. 4, with color convention stated in the caption of Fig. 3. A reduction of the cross section by about 34% with respect to the case without OREF (namely, $A = 0$ in Fig. 2 for which R_0 is reported) is observed. It is worth observing that such a reduction is obtained without altering the rheological properties of the jet by, say, changing the polymer concentration. This is comparable with similar results obtained by blowing-assisted electrospinning, where a gas stream, provided by suitable distributors around the nozzle, is employed as an additional stretching force.[30–32] The latter technique was recently extended by Sinha-Ray *et al.*[33] to include a supersonic blowing gaseous stream in electrospinning producing ultra-thin nanofibers.

Even though the functional relation $R = R(\omega)$ is the result of a highly complex structural dynamics, the oscillatory

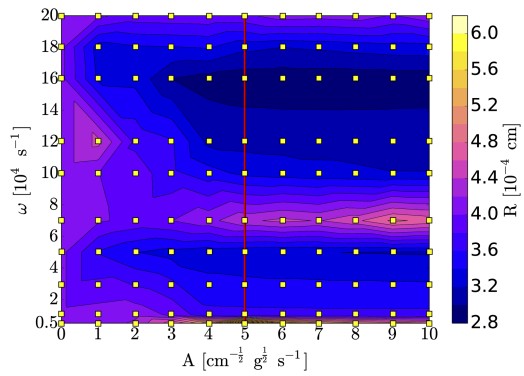

FIG. 2. Contour lines showing the simulated mean jet radius R at the collector as a function of $A \in [0, 10]$ and $\omega \in [0.5, 20]$ parameters. The $R(A, \omega)$ surface was assessed by a linear interpolation over a grid of pairs of A and ω, shown in the figure as yellow square symbols.

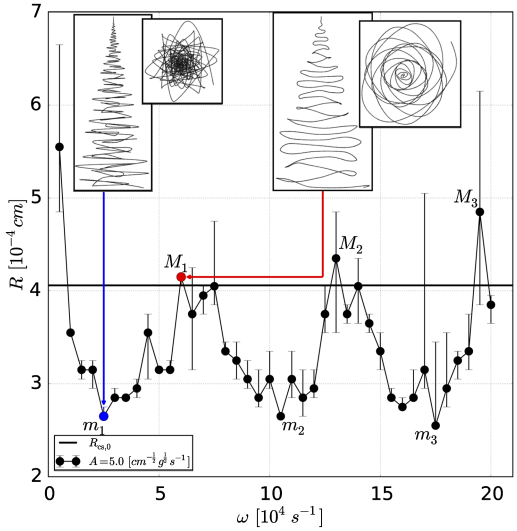

FIG. 3. Mean of cross section radius R at the collector for $A = 5$ at several values of ω, plotted with their respective interquartile as confidence intervals. The thick solid black horizontal line represents R_0, i.e., the mean value of R in a standard electrospinning process (without OREF). The first minimum and maximum of R are highlighted in red, with the insets showing the trajectories from the lateral and bottom planes.

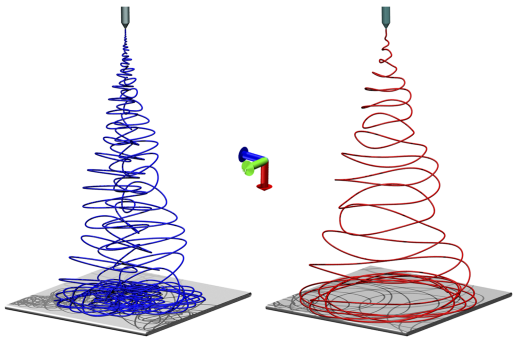

FIG. 4. Jet trajectories with $A = 5$, $\omega(m_1) = 2.5 \cdot 10^4$ s^{-1} (left blue curve), and $\omega(M_1) = 6 \cdot 10^4$ s^{-1} (right red curve). Axis convention, shown in the center, is as follows: red for the x axis, green for the y axis, and blue for the z axis. While the red curve is wider than the blue one, the latter appears more twisted, thus producing a thinner R (cf. with Figs. 2 and 3).

structure of such a relation is relatively regular and suggestive of a sort of resonant mechanism underlying the OREF setup, which is likely to depend on the frequency ω_{noz} of the mechanical oscillation of the nozzle. Here, we have kept ω_{noz} at a fixed value because it is practically easier to change the OREF frequency than modifying the inherent mechanical oscillations of the nozzle.

Nonetheless, we repeat the simulations corresponding to the two points m_1 and M_1 in Fig. 3, with a nozzle perturbation $\omega_{noz} = 2.5 \cdot 10^4$ s^{-1}. In both cases, we observe a change in the mean cross section radius $\langle R \rangle$ between 5% and 10%, compared to the previous values, confirming that both frequencies ω and ω_{noz} contribute to the oscillatory jet dynamics. At the moment, we have no clear theoretical explanation for such an oscillatory behavior that depends on the overall non-linear dynamics of the jet. However, we can define suitable observables which help elucidating the effects of the OREF on the jet morphology (see Subsection III B).

B. Statistical analysis and overlap of trajectories

Here, we provide both statistical and time-dependent analyses performed over the trajectories related to the most relevant ω values identified in Subsections III B and III C. Each jet trajectory is the result of a complex dynamics, which presents an initial drift in the time lapse where the filament has not yet reached the collector. After such a time lapse, the trajectory regularizes and consequently it becomes possible to analyze the statistical distribution of the cross section radius.

The top part of Fig. 5 shows normalized histograms for the distribution of cross section radius at the collector for three different frequencies, $\omega = [2.5, 5.5, 6] \cdot 10^4$ s^{-1}, all with the same amplitude $A = 5$ g$^{\frac{1}{2}}$cm$^{-\frac{1}{2}}$s^{-1}.

It is apparent that the frequency distribution is skewed and strongly non-Gaussian, which is relatively unsurprising due to the highly non-linear nature of the process. Owing to this non-Gaussianity, this observable is best described via its median and confidence interval (given by the first and third quartiles), as reported in Fig. 3. In order to clarify the trend of the mean radius reported in Fig. 5, we define the jet length as

$$\Lambda(t) = \sum_{i=1}^{n-1} |\vec{\mathbf{r}}_{i+1} - \vec{\mathbf{r}}_i|, \tag{7}$$

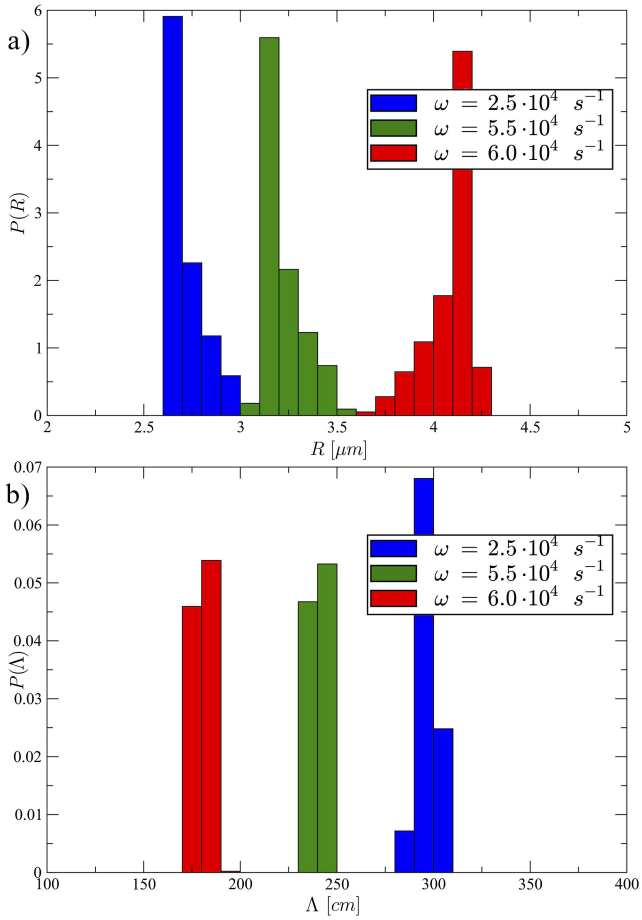

FIG. 5. Top: the normalized histograms for distribution of cross section radius R at the collector for $A = 5$ and three values of ω. Note that the distribution of the observable during the dynamics is strongly skewed and non-gaussian. Bottom: the corresponding normalized histograms for distribution of jet path length Λ, showing an opposite trend with respect to $\langle R \rangle$.

which measures the total length of the jet, from the collector up to the nozzle. Comparing the two trends of R and Λ in Fig. 5, it is apparent that the two are anti-correlated, namely, the smallest $\langle R \rangle$ corresponds to the longest $\langle \Lambda \rangle$ and vice versa. As a result, one of the main effects of OREF is to alter the jet path, which in turn modifies the jet stretch and the resulting cross sectional radius.

To gain further insights into the jet dynamics, it is also of interest to assess the "morphological distance" between two spirals corresponding to minimum and maximum fiber radii. Instead of a "smooth" Euclidean distance, we find it more informative to introduce an overlap distance between two trajectories α and β by gaining insight from an order parameter usually exploited in the context of glassy materials (see Refs. 34–36), which is defined as follows:

$$Q_{\alpha\beta}(t, \varepsilon) = \int_0^1 \Theta\left(\varepsilon - |\vec{r}_\alpha(t, \lambda) - \vec{r}_\beta(t, \lambda)|\right) d\lambda. \tag{8}$$

In the above, λ is the curvilinear coordinate, Θ is the Heaviside step function, and ε (cm) is the *distance* tolerance. The Heaviside step function acts like a switch, turning off whenever the distance of two homologue points with the same λ at two different jets goes above a given threshold ε. Therefore, $Q_{\alpha\beta}$ serves as a suitable indicator of the *separation transition*

between two indistinguishable ($Q = 1$) and two fully separated ($Q = 0$) configurations, at the given scale ε. Note that by assuming the jet discretized as a set of n parcels, each parcel can only contribute a factor $1/n$ to the overlap parameter. This is in contrast with the Euclidean distance which may eventually be completely dominated by a single, localized, large deviation between the two jets. Being sensitive to the value of ε, Q is a useful indicator of the dynamics of the separation process at different scales.

We evaluated the overlap distance for three values of the parameter ε as a function of time t and correlate this indicator with $R(M_1)$ and $R(m_1)$. As a reference value, we take $\varepsilon_{\text{ref}} = 0.94$ cm, i.e., the pitch distance of the jet-path in the case m_1 (see the insets of Fig. 3). Our results pertain to $\alpha \equiv m_1$ and $\beta \equiv M_1$, in Fig. 6, where a separation transition between the two jets is apparent. By definition, for $\varepsilon = 0$, the two jets are always separated so that $Q_{m_1M_1} = 0$ at all times.

On the other hand, at increasing ε, the two jets overlap only up to an initial time t_{ov}, while for $t > t_{ov} \sim 0.01$ s, a separation transition starts to take place, with the two jets getting more separated as ε is made smaller. After $t = 0.15$ s, the distance between the two configurations reaches its asymptotic value. On top of Fig. 6, we report some snapshots of the two jets at a given time, to provide a visual counterpart of the corresponding values of $Q_{m_1M_1}(t, \varepsilon)$.

C. Time series analysis of trajectories

In order to gain further insight into the jet dynamics, we analyze the frequency spectra induced by OREF on the jet dynamics. In particular, the Fourier analysis exposes the frequencies of the swirling motion of the helix, which has a direct bearing on the jet path and the resulting fiber radius.

To this purpose, let us consider a plane perpendicular to the *x-axis* placed at $x = 8$ cm and denote it by $\vec{v}^*_\perp = v_y(\lambda|x = 8\text{ cm})\vec{u}_y + v_z(\lambda|x = 8\text{ cm})\vec{u}_z$, the projection on this plane of the velocity vector measured at the point λ where the jet crosses such plane.

We inspect the normalized velocity autocorrelation function (VACF) of $\vec{v}^*_\perp$ defined as

$$Z(\tau) = \langle \vec{v}^*_\perp(t) \cdot \vec{v}^*_\perp(t+\tau)\rangle_t / \langle \vec{v}^*_\perp(t) \cdot \vec{v}^*_\perp(t)\rangle_t, \qquad (9)$$

where brackets denote time-averaging over the corresponding steady-state regime. The quantity $Z(\tau)$ measures the self-correlation of the swirling motion within the jet path. Then, cosine Fourier transformation (power spectra) of the VACF was computed for each OREF frequency, in order to expose the spectral densities of states.[37]

We focus our attention on three main cases: first, the simulation setup without OREF as a reference case. The second and third correspond to the simulation setups denoted by m_1 and M_1, respectively, in Fig. 3. In Fig. 7, we observe a central peak at 1600 Hz for all three cases under

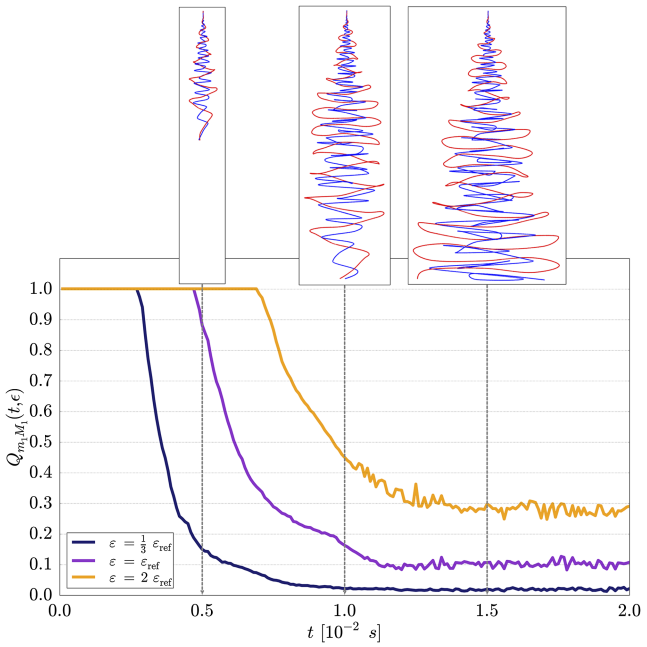

FIG. 6. Overlapping function $Q_{m_1M_1}(t, \varepsilon)$ as a function of time, for three values of ε. For non-zero values of ε, an abrupt transition is evident, which stops after the drift time t_{drift} has been reached. In particular, the smaller the value of ε, the smaller $Q(\varepsilon, t)$ is. Snapshots of the two jets analyzed at three times are reported in the insets over the plot, where color legend is the same as Fig. 4. We wish to remark that the trajectories should not self-intersect and they actually do not.

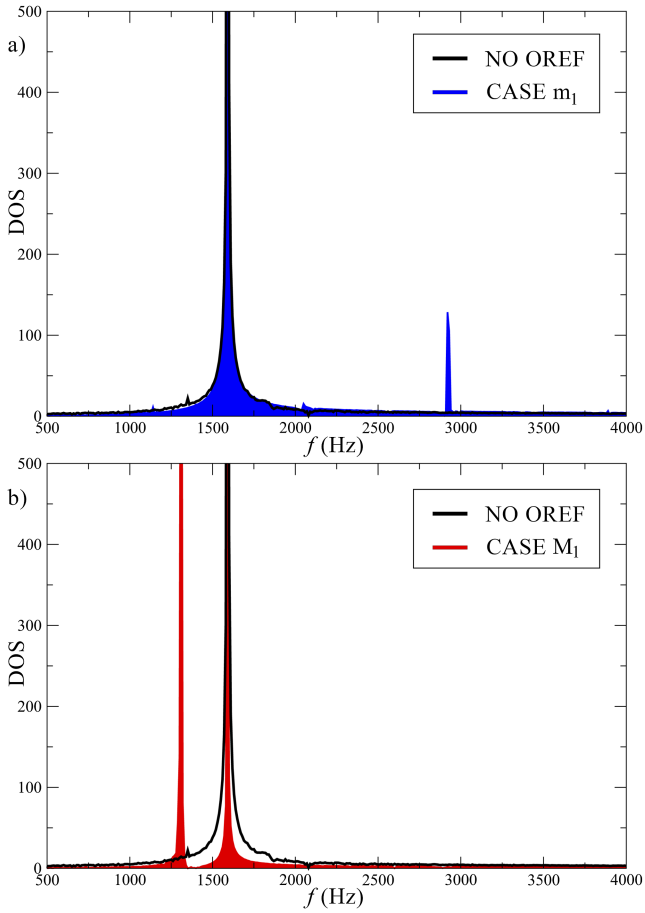

FIG. 7. Cosine Fourier transformation (density of states) of the VACF computed for the three cases: without OREF as a reference case (drawn in black line), with OREF at $\omega(m_1) = 2.5 \cdot 10^4$ s^{-1} (blue curve on the top panel), and $\omega(M_1) = 6 \cdot 10^4$ s^{-1} (red curve on the bottom panel). We observe as the case m_1 corresponds to the presence of a second peak located at higher frequency, while the case M_1 is characterized by a second peak detected at lower frequency.

inspection, which is related to the main swirling motion resulting from the mechanical oscillation of the nozzle. Upon switching-on the OREF, satellite peaks are seen to appear, at higher (lower) frequencies for the case m_1 and M_1, respectively.

In order to elucidate the relation between the jet path $\langle\Lambda\rangle$ and the frequency of the secondary peak in the power spectra, we invoke simple arguments related to the helicoidal motion of jet.

For the sake of simplicity, we assume (neglecting other terms as Coulomb repulsive forces, etc.) that the centrifugal force of the ith jet segment is approximately given by $F_{C,i} \propto q_i A$, where A is the OREF amplitude, laid on the plane of rotation, and q_i is the net charge of the jet segment. The corresponding curvature radius is $r_{c,i} \propto (q_i A)/(m_i \omega_f^2)$, where m_i is the mass of the jet segment and ω_f is the angular swirling frequency reported in Fig. 7. Further, we can assess the pitch of the jet helix, defined as the height of a complete helix turn, $h_i = 2\pi v_{x,i}/\omega_f$, where $v_{x,i}$ is the velocity component of the ith jet segment along the x axis.

A number of considerations on the jet path and swirling frequency arise from the above relations. In particular, we note that the second peak in power spectra located at higher frequency provides a reduction of the helix pitch and an increase of the jet curvature, which is the reciprocal of the curvature radius. As a consequence, the number of helices drawn by the jet between the nozzle and the collector significantly increases, thereby providing a larger value of the jet path length Λ observed in Fig. 5. Furthermore, we observe that the OREF can also be used as a tool to control the jet curvature and possibly drive the jet deposition on the collector, as detailed in Subsection III D.

D. Statistical analysis of jet deposition at the collector

The OREF significantly affects the spatial distribution of the jet, providing several patterns of the electrospun coatings deposited on the collector. In Fig. 8, we report the normalized 2D maps, showing the probability of a jet parcel to hit the collector at the coordinates y and z (both perpendicular to x by construction). Note that only the late dynamics describing the stationary regime was considered in order to compute the histograms. Here, we observe a clear modification of the pattern deposition as a function of the applied OREF frequency ω. In particular, by tuning the frequency, the deposition pattern is driven towards the inner region of the collector.

This is evident in the top panel of Fig. 8, where we report the normalized histogram for the case m_1, with the probability distribution spanning over a precession motion. This is likely due to the combined effects of the two peaks in the frequency spectra (see Fig. 7). Since the second peak is located at higher frequency, we observe a tighter deposition due to the larger jet curvature, depending on the frequency as shown in Fig. 8. On the other hand, if the second frequency lies below the one of the precession motion, the distribution stretches towards the external region of the collector.

Therefore, the OREF frequency ω appears to offer new, possibly even time-dependent, strategies to achieve uniform distributions at the collector plate.

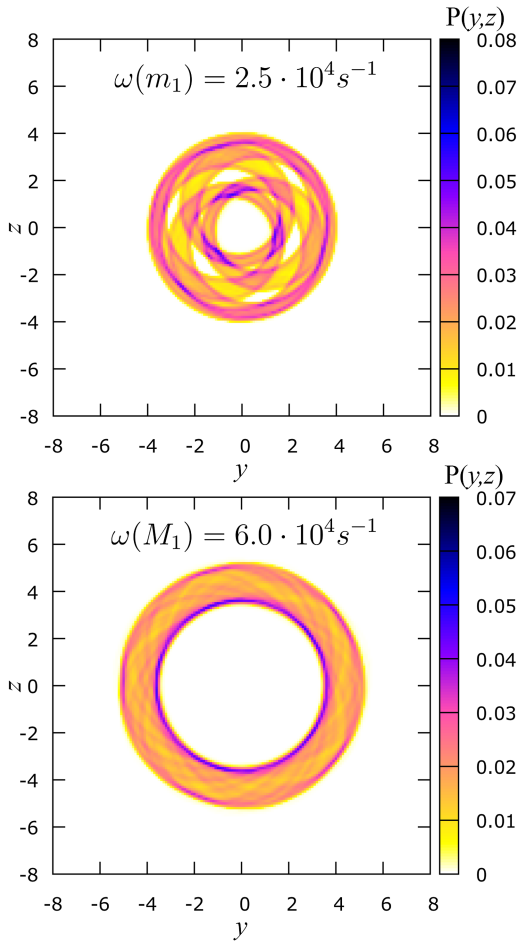

FIG. 8. Normalized 2D maps computed over the coordinates y and z of the collector for the two cases with OREF at $\omega(m_1)$ (on top panel) and $\omega(M_1)$ (on bottom panel). The color palettes define the probability that a jet parcel hits the collector in coordinates y and z.

IV. SUMMARY AND OUTLOOK

Summarizing, we have proposed the OREF mechanism and explored its effects on the electrospinning process, particularly on the radius of the electrospun fibers. Numerical simulations using the JETSPIN code show that such a radius can be reduced up to about 30%. Despite the inherent complexity of the underlying dynamics, the electrospinning response to OREF $R = R(\omega)$ appears to organize into a rather regular oscillatory pattern, with periodic local minima and maxima of the finer radius as a function of the OREF frequency. The existence of such minima opens up the possibility of advancing electrospinning technologies and producing finer fibers with high repeatability. Further, the OREF can be used as a control mechanism to achieve uniform distributions of polymer filaments at the collector.

While a 30% reduction of the diameter of single nanofibers might not seem that dramatic, controlling the morphology of electrospun materials in such a finer way might prove useful. For instance, the fraction of power of the fundamental mode of a cylindrical waveguide strongly (exponential-like) depends on the diameter of the guide, with a 30% variation of the diameter potentially leading to a significant (e.g., 20%) change of coupled optical power.[38] Also, fibers with such

reduced size being most sensitive to their external environment might lead to changes of their refractive index due to detected chemical or biological species, which can be probed by variations in the power transmitted in single nanofiber waveguides. Finally, more uniform area coverage can lead to better coatings and improved filtrating materials. These perspectives are intriguing and worth experimental investigation.

The present simulations permit to highlight the salient morpho-dynamical features associated with the application of the OREF, as well as to probe the electrospinning response in a range of applied frequencies. Much remains to be done for the future; particularly, the study of the spatial dependence of the self-consistent electrostatic field induced by charge deposition at the collector and its effects on the overall jet dynamics and associated deposition patterns. Moreover, a fully fledged analysis of the non-linear dynamical behavior of the OREF setup would be highly desirable. Studies along these lines are currently under way.

ACKNOWLEDGMENTS

The research leading to these results has received funding from the European Research Council under the European Union's Seventh Framework Programme (No. FP/2007-2013)/ERC Grant Agreement No. 306357 (NANO-JETS).

[1] D. Li, Y. Wang, and Y. Xia, "Electrospinning nanofibers as uniaxially aligned arrays and layer-by-layer stacked films," Adv. Mater. **16**, 361–366 (2004).
[2] A. Greiner and J. H. Wendorff, "Electrospinning: A fascinating method for the preparation of ultrathin fibers," Angew. Chem., Int. Ed. **46**, 5670–5703 (2007).
[3] C. P. Carroll and Y. L. Joo, "Axisymmetric instabilities of electrically driven viscoelastic jets," J. Non-Newtonian Fluid Mech. **153**, 130–148 (2008).
[4] Z.-M. Huang, Y. Z. Zhang, M. Kotaki, and S. Ramakrishna, "A review on polymer nanofibers by electrospinning and their applications in nanocomposites," Compos. Sci. Technol. **63**, 2223–2253 (2003).
[5] A. L. Yarin, B. Pourdeyhimi, and S. Ramakrishna, *Fundamentals and Applications of Micro and Nanofibers* (Cambridge University Press, 2014).
[6] J. H. Wendorff, S. Agarwal, and A. Greiner, *Electrospinning: Materials, Processing, and Applications* (John Wiley & Sons, 2012).
[7] D. Pisignano, *Polymer Nanofibers: Building Blocks for Nanotechnology*, Vol. 29 (Royal Society of Chemistry, 2013).
[8] A. L. Yarin, S. Koombhongse, and D. H. Reneker, "Bending instability in electrospinning of nanofibers," J. Appl. Phys. **89**, 3018–3026 (2001).
[9] M. M. Hohman, M. Shin, G. Rutledge, and M. P. Brenner, "Electrospinning and electrically forced jets. I. Stability theory," Phys. Fluids **13**, 2201–2220 (2001).
[10] A. M. Ganan-Calvo, "On the theory of electrohydrodynamically driven capillary jets," J. Fluid Mech. **335**, 165–188 (1997).
[11] A. Huebner and H. Chu, "Instability and breakup of charged liquid jets," J. Fluid Mech. **49**, 361–372 (1971).
[12] D. H. Reneker, A. L. Yarin, H. Fong, and S. Koombhongse, "Bending instability of electrically charged liquid jets of polymer solutions in electrospinning," J. Appl. Phys. **87**, 4531–4547 (2000).
[13] M. Lauricella, D. Pisignano, and S. Succi, "Three-dimensional model for electrospinning processes in controlled gas counterflow," J. Phys. Chem. A **120**, 4884–4892 (2016).
[14] C. P. Carroll and Y. L. Joo, "Discretized modeling of electrically driven viscoelastic jets in the initial stage of electrospinning," J. Appl. Phys. **109**, 094315 (2011).
[15] A. M. Ganan-Calvo, J. C. Lasheras, J. Dávila, and A. Barrero, "The electrostatic spray emitted from an electrified conical meniscus," J. Aerosol Sci. **25**, 1121–1142 (1994).
[16] W. Yang, H. Duan, C. Li, and W. Deng, "Crossover of varicose and whipping instabilities in electrified microjets," Phys. Rev. Lett. **112**, 054501 (2014).
[17] S. N. Reznik and E. Zussman, "Capillary-dominated electrified jets of a viscous leaky dielectric liquid," Phys. Rev. E **81**, 026313 (2010).
[18] D. H. Reneker and A. L. Yarin, "Electrospinning jets and polymer nanofibers," Polymer **49**, 2387–2425 (2008).
[19] S. V. Fridrikh, J. H. Yu, M. P. Brenner, and G. C. Rutledge, "Controlling the fiber diameter during electrospinning," Phys. Rev. Lett. **90**, 144502 (2003).
[20] M. Lauricella, G. Pontrelli, I. Coluzza, D. Pisignano, and S. Succi, "JETSPIN: A specific-purpose open-source software for simulations of nanofiber electrospinning," Comput. Phys. Commun. **197**, 227–238 (2015).
[21] M. Lauricella, G. Pontrelli, D. Pisignano, and S. Succi, "Dynamic mesh refinement for discrete models of jet electro-hydrodynamics," J. Comput. Sci. **17**, 325–333 (2016).
[22] T. A. Kowalewski, S. Barral, and T. Kowalczyk, "Modeling electrospinning of nanofibers," in *IUTAM Symposium on Modelling Nanomaterials and Nanosystems*, *Aalborg*, *Denmark*, *May 19–22, 2008*, edited by R. Pyrz and J. C. Rauhe (Springer, 2009), **13**, pp. 279–292.
[23] Y. Sun, Y. Zeng, and X. Wang, "Three-dimensional model of whipping motion in the processing of microfibers," Ind. Eng. Chem. Res. **50**, 1099–1109 (2010).
[24] X. P. Huang, F. Anderegg, E. M. Hollmann, C. F. Driscoll, and T. M. O'neil, "Steady-state confinement of non-neutral plasmas by rotating electric fields," Phys. Rev. Lett. **78**, 875 (1997).
[25] M. Montinaro, V. Fasano, M. Moffa, A. Camposeo, L. Persano, M. Lauricella, S. Succi, and D. Pisignano, "Sub-ms dynamics of the instability onset of electrospinning," Soft Matter **11**, 3424–3431 (2015).
[26] N. Yuya, W. Kai, B. S. Kim, and I. S. Kim, "Morphology controlled electrospun poly(vinyl pyrrolidone) fibers: Effects of organic solvent and relative humidity," J. Mater. Sci. Eng. Adv. Technol. **2**, 97–112 (2010).
[27] V. N. Morozov and A. Y. Mikheev, "Water-soluble polyvinylpyrrolidone nanofilters manufactured by electrospray-neutralization technique," J. Membr. Sci. **403-404**, 110–120 (2012).
[28] V. Bühler, *Polyvinylpyrrolidone Excipients for Pharmaceuticals: Povidone, Crospovidone and Copovidone* (Springer Science & Business Media, 2005).
[29] A. L. Yarin, *Free Liquid Jets and Films: Hydrodynamics and Rheology* (Longman Scientific & Technical Harlow, 1993).
[30] X. Wang, I. C. Um, D. Fang, A. Okamoto, B. S. Hsiao, and B. Chu, "Formation of water-resistant hyaluronic acid nanofibers by blowing-assisted electro-spinning and non-toxic post treatments," Polymer **46**, 4853–4867 (2005).
[31] Y. Lin, Y. Yao, X. Yang, N. Wei, X. Li, P. Gong, R. Li, and D. Wu, "Preparation of poly(ether sulfone) nanofibers by gas-jet/electrospinning," J. Appl. Polym. Sci. **107**, 909–917 (2008).
[32] H. Y. Hsiao, C. M. Huang, Y. Y. Liu, Y. C. Kuo, and H. Chen, "Effect of air blowing on the morphology and nanofiber properties of blowing-assisted electrospun polycarbonates," J. Appl. Polym. Sci. **124**, 4904–4914 (2012).
[33] S. Sinha-Ray, M. W. Lee, S. Sinha-Ray, S. An, B. Pourdeyhimi, S. S. Yoon, and A. L. Yarin, "Supersonic nanoblowing: A new ultra-stiff phase of nylon 6 in 20–50 nm confinement," J. Mater. Chem. C **1**, 3491–3498 (2013).
[34] M. Ozawa, W. Kob, A. Ikeda, and K. Miyazaki, "Equilibrium phase diagram of a randomly pinned glass-former," Proc. Natl. Acad. Sci. U. S. A. **112**, 6914–6919 (2015).
[35] W. Kob and L. Berthier, "Probing a liquid to glass transition in equilibrium," Phys. Rev. Lett. **110**, 245702 (2013).
[36] T. R. Kirkpatrick, D. Thirumalai, and P. G. Wolynes, "Scaling concepts for the dynamics of viscous liquids near an ideal glassy state," Phys. Rev. A **40**, 1045 (1989).
[37] M. P. Allen and D. J. Tildesley, *Computer Simulation of Liquids* (Oxford university press, 1989).
[38] V. Fasano, A. Polini, G. Morello, M. Moffa, A. Camposeo, and D. Pisignano, "Bright light emission and waveguiding in conjugated polymer nanofibers electrospun from organic salt added solutions," Macromolecules **46**, 5935–5942 (2013).